Check for updates

Earth and Space Science

RESEARCH ARTICLE
10.1029/2026EA005334

# A Geophysical Crustal Model of Central Italy for Geoneutrino Predictions in Borexino

**L. Rossi[1], M. Capponi[2], P. Conti[3], N. I. Elek[4,5], A. Ermini[3,6], K. G. C. Raptis[4,5], M. Reguzzoni[1], V. Strati[4,5], M. M. Tiberti[7], F. E. Maesano[7], R. Maffucci[7], M. Buttinelli[7], M. Abdelkader[4,5], M. Albèri[4,5], A. Albertella[1], G. Hasnain[4,5,6], F. Mantovani[4,5], L. Pagano[4,5], S. Ramouz[1], R. Salvini[3], D. Sampietro[2,8], and P. S. Dinani[3]**

[1]Department of Civil and Environmental Engineering (DICA), Politecnico di Milano, Milan, Italy, [2]Geomatics Research & Development, Lomazzo, Italy, [3]Department of Physical Sciences, Earth and Environment and Centre of Geotechnologies CGT, University of Siena, San Giovanni Valdarno, Italy, [4]Department of Physics and Earth Sciences, University of Ferrara, Ferrara, Italy, [5]INFN Ferrara Section, Ferrara, Italy, [6]University of Trento, Trento, Italy, [7]Istituto Nazionale di Geofisica e Vulcanologia (INGV), Rome, Italy, [8]Istituto Nazionale di Geofisica e Vulcanologia, Sezione di Catania - Osservatorio Etneo, Catania, Italy

**Key Points:**

- GUESS: a new probabilistic 3-D crustal model for the Gran Sasso region, built by Bayesian inversion of gravity, seismic, and borehole data
- Posterior densities validated against three independent benchmarks
- Structural uncertainty on the geoneutrino signal constrained to 1%–3%

**Supporting Information:**

Supporting Information may be found in the online version of this article.

**Correspondence to:**

V. Strati,
strati@fe.infn.it

**Citation:**

Rossi, L., Capponi, M., Conti, P., Elek, N. I., Ermini, A., Raptis, K. G. C., et al. (2026). A geophysical crustal model of central Italy for geoneutrino predictions in Borexino. *Earth and Space Science*, *13*, e2026EA005334. https://doi.org/10.1029/2026EA005334

Received 5 JUN 2026
Accepted 4 OCT 2026

**Author Contributions:**

**Conceptualization:** L. Rossi, P. Conti, A. Ermini, M. Reguzzoni, V. Strati, M. M. Tiberti, F. E. Maesano, R. Maffucci, M. Buttinelli, F. Mantovani, R. Salvini
**Data curation:** F. E. Maesano, R. Maffucci, M. Albèri, S. Ramouz, D. Sampietro, P. S. Dinani
**Formal analysis:** L. Rossi, M. Capponi, K. G. C. Raptis, V. Strati
**Funding acquisition:** L. Rossi, V. Strati, L. Pagano, R. Salvini
**Investigation:** N. I. Elek, K. G. C. Raptis, V. Strati, G. Hasnain, S. Ramouz
**Methodology:** L. Rossi, M. Capponi, M. Reguzzoni, V. Strati, F. Mantovani
**Project administration:** L. Rossi, V. Strati, L. Pagano

© 2026 The Author(s). Earth and Space Science published by Wiley Periodicals LLC on behalf of American Geophysical Union.
This is an open access article under the terms of the Creative Commons Attribution License, which permits use, distribution and reproduction in any medium, provided the original work is properly cited.

**Abstract** Predicting the geoneutrino signal at underground detectors requires a local crustal reference whose precision matches the experimental uncertainty. The current Borexino reference is 15 years old and deterministic. We replace it with GUESS, a probabilistic 3-D model of the Gran Sasso region, built by Bayesian inversion of multi-source geophysical data: ground and satellite gravity, deep exploration wells, seismic profiles, receiver-function Moho constraints, and high-resolution topography are fused into a posterior distribution of density and lithological label per voxel. The model partitions the volume into six lithologically distinct units, each with quantified uncertainty on volume, mass and average density, and is validated against three independent in situ density benchmarks. The structural uncertainty on the predicted geoneutrino signal of the major units is constrained to 1%–3%, an order of magnitude below the uncertainty on uranium and thorium abundances. The dominant source of error in the absolute crustal geoneutrino prediction therefore shifts from crustal geometry to elemental composition, defining the next priority for the Borexino determination of the radiogenic heat budget.

**Plain Language Summary** Deep inside the Earth, naturally occurring radioactive elements (uranium, thorium, and potassium) continuously decay and release heat, contributing to plate tectonics and other geological processes. A small fraction of these decays produces particles called geoneutrinos, which travel through rock unimpeded and can be detected with specialized detectors deep underground. The Borexino experiment, under the Gran Sasso massif in central Italy, measured these particles for over 14 years. Correctly interpreting its measurements and estimating the Earth's radioactive heat budget requires an accurate model of the local rocks, because most of the detected signal comes from within a few hundred kilometers of the detector. We built GUESS, a new three-dimensional model of the Earth's crust in the Gran Sasso region. Unlike earlier single-value reconstructions, GUESS combines satellite and ground gravity measurements, deep borehole logs, seismic profiles, and crustal thickness constraints through a statistical approach, so every geological layer carries a quantified uncertainty. Our results show that the geometric uncertainty of the model contributes only 1%–3% to the geoneutrino signal prediction, far smaller than the uncertainty in the uranium and thorium content of the rocks.

## 1. Introduction

Geoneutrinos (electron antineutrinos from beta decays of Heat-Producing Elements, HPEs: K, Th, U) are a direct probe of the radioactive content of the deep Earth. Each decay releases an antineutrino-to-heat ratio fixed by nuclear physics, so the geoneutrino flux measured at the surface fixes the radiogenic heat budget when interpreted within a known geological framework (Bellini et al., 2021; Fiorentini et al., 2007). Liquid scintillator detectors are not directional, so crustal and mantle contributions cannot be separated at a single site: the global distribution of HPEs can emerge only from a multi-site analysis combining detectors at different geological settings (Bellini et al., 2021).

The $1/r^2$ attenuation makes the crustal signal at any site dominated by sources within a few hundred kilometers from the detector. This sets the scale of the modeling problem: a high-resolution local model is required to

**Resources:** L. Rossi, P. Conti, V. Strati, M. M. Tiberti, F. E. Maesano, R. Maffucci, M. Buttinelli, R. Salvini
**Software:** L. Rossi, M. Capponi, K. G. C. Raptis, M. Reguzzoni, V. Strati, D. Sampietro, P. S. Dinani
**Supervision:** L. Rossi, V. Strati, A. Albertella, F. Mantovani, L. Pagano
**Validation:** L. Rossi, M. Capponi
**Visualization:** N. I. Elek, A. Ermini, K. G. C. Raptis, M. Abdelkader
**Writing – original draft:** L. Rossi, P. Conti, K. G. C. Raptis, M. Reguzzoni, V. Strati, M. M. Tiberti, F. E. Maesano, M. Buttinelli, F. Mantovani, R. Salvini
**Writing – review & editing:** L. Rossi, M. Capponi, P. Conti, N. I. Elek, A. Ermini, K. G. C. Raptis, M. Reguzzoni, V. Strati, M. M. Tiberti, F. E. Maesano, R. Maffucci, M. Buttinelli, M. Abdelkader, M. Albèri, A. Albertella, G. Hasnain, F. Mantovani, L. Pagano, R. Salvini

subtract the near-field crustal contribution and isolate the mantle component, while finer geological detail at sub-kilometer scale is invisible to the integrated flux and a coarser regional model misses the local mass distribution. The model resolution must match the spatial response of the signal, not the resolution of available geological maps.

The geoneutrino detectors network now spans KamLAND (Araki et al., 2005), Borexino (Bellini et al., 2010), SNO+ (Allega et al., 2025), and JUNO which has recently entered the data-taking phase (Abusleme et al., 2022). Site-specific crustal references have been built for KamLAND (Enomoto et al., 2007), Borexino (Coltorti et al., 2011), SNO+ (Huang et al., 2014; Strati et al., 2017), and JUNO (Gao et al., 2020; Reguzzoni et al., 2019). After 14 years of operation, Borexino reached an experimental uncertainty of 18% on the geoneutrino flux (Agostini et al., 2020); matching this measurement precision requires a corresponding refinement of the local crustal model used to subtract the near-field contribution. The reference Borexino model (Coltorti et al., 2011) is now 15 years old. Two main developments have transformed the input space since then: dense teleseismic monitoring, including the 2016–2017 Central Italy seismic sequence, has refined the Moho geometry (Piana Agostinetti et al., 2022; Spada et al., 2013) and Bayesian gravity inversion, deployed on JUNO (Reguzzoni et al., 2019) and KamLAND (Takeuchi et al., 2019), now enables probabilistic data fusion with quantified uncertainty on subsurface mass distribution. The Bayesian framework also accommodates high-resolution topography, which is critical for U and Th mass estimates near the detector (Strati et al., 2020).

We present GUESS (GeoneUtrinos: mESSengers of the Earth's interior), a 3-D probabilistic crustal model of a $3° \times 3°$ region centered on the Laboratori Nazionali del Gran Sasso (LNGS, L'Aquila, Italy), where Borexino has operated. The voxel size is $4 \times 4 \times 0.1$ km. GUESS integrates, within a Bayesian inversion framework, (a) ground and satellite gravity (XGM2019e), (b) high-resolution topography (TINITALY 100 m), (c) 53 deep exploration wells, (d) 38 cross-sections from CROP and RETRACE-3D projects (Buttinelli et al., 2021; Di Bucci et al., 2021), and (e) 154 Moho depth points. The output partitions the volume into six GUESS units (Quaternary volcanics, Cenozoic terrigenous sediments, Mesozoic carbonates, Permian-Triassic succession, Upper Crust [UC], and Lower Crust [LC]), each with quantified uncertainty on volume, mass and average density. Posterior densities are validated against independent sonic-log data sets (Montone & Mariucci, 2020, 2026; Tiberti et al., 2026). The structural uncertainty propagated to the predicted geoneutrino signal is constrained to 1%–3% for the major units, shifting the dominant source of error from crustal geometry to U and Th abundance. The model is publicly available at www.fe.infn.it/radioactivity/GUESS/.

## 2. Materials and Methods

### 2.1. Geological Setting of the Region

The study area covers a $3° \times 3°$ region centered on the Borexino detector (N 42.45°, E 13.57°, 960 m a.s.l.), an underground liquid scintillator that operated from 2007 to 2021 (Bellini, 2024). The detector is hosted by the Laboratori Nazionali del Gran Sasso (LNGS), shielded by 1,400 m of rock under the Gran Sasso massif (Capuano et al., 1998).

The Apennines orogenic belt formed during the Neogene-Quaternary closure of the Tethyan oceanic basin (Vai & Martini, 2001), with a subsequent back-arc extension producing the asymmetric crustal thickness pattern observed today: 12–30 km below the Tyrrhenian sector and 30–44 km below the Adriatic foreland (Di Stefano et al., 2011; Spada et al., 2013). The boundary, dipping westward across the study area, is imaged in the CROP03, CROP04 and CROP11 deep seismic profiles (Barchi et al., 1998; Di Luzio et al., 2009; Feriozzi et al., 2024; Finetti et al., 2001; Scrocca et al., 2007). Its shallower portion is a low-angle detachment at the base of the Mesozoic carbonate units. The Gran Sasso massif sits above this regional discontinuity, placing Borexino at the geometric center of the Adria-Tyrrhenian transition zone. Beneath the axial belt, the Tyrrhenian Moho overlies the Adriatic Moho along a continuous overlap zone, interpreted as the locus of ongoing lower-crustal delamination (Tavani et al., 2026).

The crust hosts two main crystalline layers, with no evidence of a middle crust in Central Italy (Cassinis et al., 2003; Finetti, 2005): the UC, locally overlain by a Permian-Triassic clastic succession (pt) of slightly metamorphic metasandstones and shales (Scrocca et al., 2007), and the LC. The sedimentary cover above the UC groups several geological units mapped in Figure 1a (Bigi et al., 1991; Conti et al., 2020; Patacca &

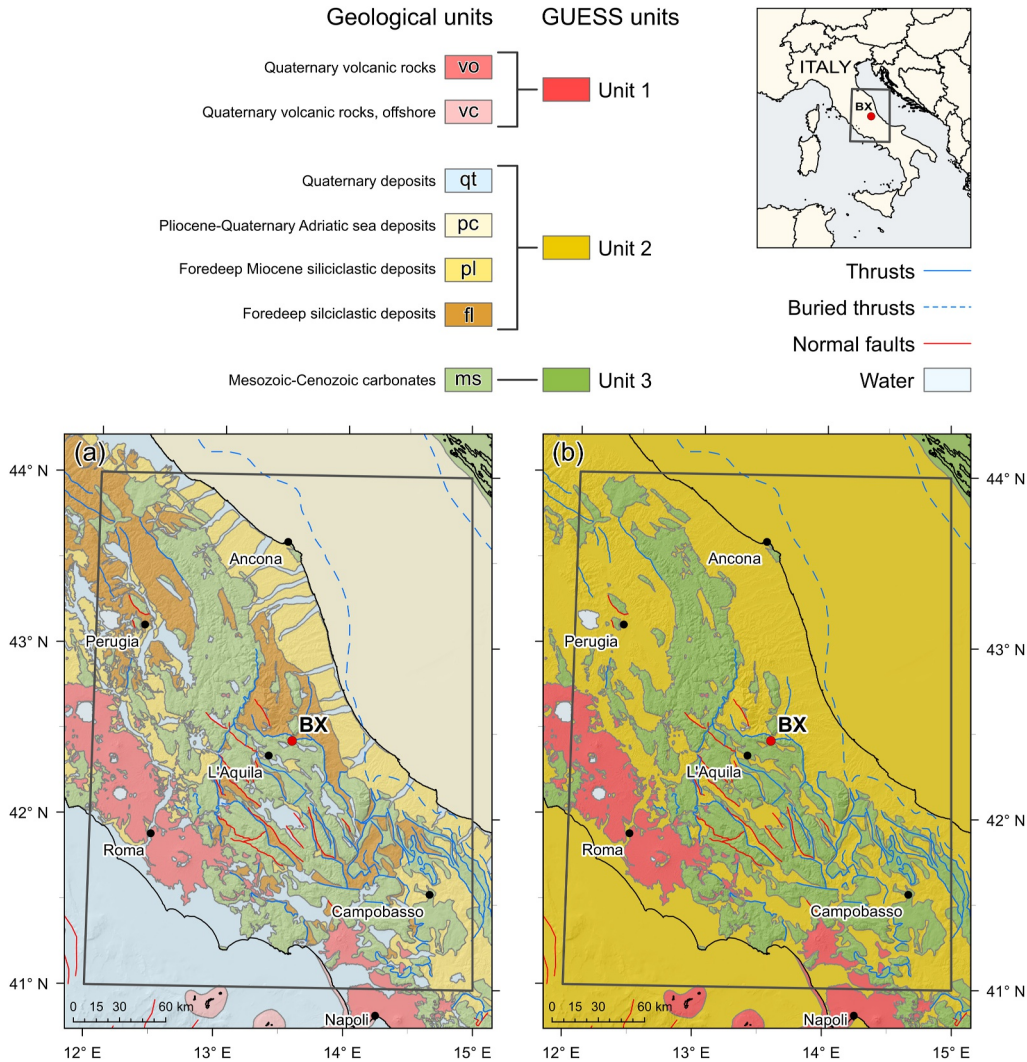



**Figure 1.** (a) Geological map of the study area, with formations grouped by lithology and depositional history. (b) Simplified surface classification into the units used by the GUESS model (volcanic rocks, terrigenous sediments, and carbonates), with major thrusts and normal faults. BX marks the Borexino detector site.

Scandone, 2007): Mesozoic carbonates (ms; limestones, dolomites, marls), Cenozoic terrigenous formations including extensional, foredeep and offshore deposits (pl, fl, pc; sandstones, clays, conglomerates), Quaternary alluvial sediments (qt), and Plio-Pleistocene potassic to ultrapotassic volcanics of the Latium-Campania provinces (vo, vc; Peccerillo, 2017). The volcanic deposits cover 6,000 $km^2$ with a volume of about 900 $km^3$ and an average thickness of 150 m. They host U and Th concentrations that exceed those of any other lithology in the area, making them disproportionately important for the geoneutrino signal despite their negligible mass fraction.

These geological units are clustered into six GUESS units (Table 1, Figure 1b) on the basis of lithology, age and bulk density. The clustering is geochemistry-driven because the geoneutrino signal of each unit depends on its U and Th content (Equation 8): Unit 1 groups all volcanics, isolating the felsic potassic suite with the highest HPE concentrations; Unit 2 (terrigenous) and Unit 3 (carbonates) split the sedimentary cover according to dominant mineralogy; Unit 4 represents the Permian-Triassic succession, set apart by its low density; Units 5 and 6 are the Upper Crust (UC) and Lower Crust (LC).

**Table 1**
*The Six GUESS Units of the 3-D Model, Derived by Clustering Geological Formations on the Basis of Lithology and Bulk Density*

| ID | GUESS unit | Geological unit | Lithologies | Age |
|---|---|---|---|---|
| 1 | Quaternary volcanic rocks | vo—Quaternary volcanic rocks<br>vc—Quaternary volcanic rocks, offshore | Volcanic complexes of potassic (trachybasalt to trachyte), shoshonitic, and ultrapotassic (leucite-tephrite to phonolite) rocks | Pleistocene-Present |
| 2 | Cenozoic terrigenous sediments | qt—Quaternary deposits<br>pc—Pliocene-Quaternary Adriatic Sea deposits<br>pl—Foredeep Miocene siliciclastic deposits<br>fl—Foredeep siliciclastic deposits | Clays, sandstones, conglomerates, shales | Miocene-Present |
| 3 | Mesozoic carbonates | ms—Meso-Cenozoic carbonates | Carbonates, dolomites, marls, shales | Mesozoic-Miocene |
| 4 | Permian-Triassic succession | pt—Continental deposits of the Permian-Triassic basins | Sandstones, conglomerates, phyllites, schists | Paleozoic-Triassic |
| 5 | Upper Crust | – | Phyllites, schists | Paleozoic-Triassic |
| 6 | Lower Crust | – | Amphibolites, gabbroes, diorites, granulites | Precambrian-Paleozoic |

*Note.* Mapping to surface geological codes (Figure 1a), lithologies and age range are reported per unit.

### 2.2. Bayesian Gravity Inversion

The Bayesian gravity inversion is a method that can be exploited for reconstructing a three-dimensional, geologically constrained model of the Earth's crust by integrating gravity observations with prior geophysical and geological information. The study volume is divided into $N$ voxels disposed on a regular grid. Each voxel is described by a mass density $\rho_i$, with $i = 1, \ldots, N$, assumed to be constant inside the voxel volume, and a label $L_i$ denoting its model unit. This setup allows the model to have neat density separations between different units, as well as introducing some geological boundary conditions directly into the inversion process.

At the basis of the inversion algorithm there is the Bayes' theorem (Box & Tiao, 1992):

$$P(\boldsymbol{x}|\boldsymbol{y}) \propto \mathcal{L}(\boldsymbol{y}|\boldsymbol{x}) \cdot P(\boldsymbol{x}) \tag{1}$$

where $\boldsymbol{x} = [\boldsymbol{\rho}, \boldsymbol{L}]$ is a vector containing the model parameters (i.e., the set of labels and densities), $y$ is the vector of observable gravity data, $P(\boldsymbol{x})$ and $P(\boldsymbol{x}|\boldsymbol{y})$ are the prior and posterior probability distributions of the model parameters, respectively, and $\mathcal{L}(\boldsymbol{y}|\boldsymbol{x})$ is the likelihood probability distribution. Because gravity is observed, the likelihood distribution measures how well a set of model parameters $x$ explains the data $y$. Assuming the observation noise to be normally distributed, the likelihood distribution is expressed as:

$$\mathcal{L}(\boldsymbol{y} = \boldsymbol{y}^o|\boldsymbol{x}) \propto \exp\left\{-\frac{1}{2}[\boldsymbol{y}^o - \boldsymbol{y}(\boldsymbol{x})]^T \mathbf{C}_{\nu\nu}^{-1}[\boldsymbol{y}^o - \boldsymbol{y}(\boldsymbol{x})]\right\} \tag{2}$$

where $\boldsymbol{y}^o$ is the vector of observed gravity values, $\mathbf{C}_{\nu\nu}$ is their noise covariance matrix, and $\boldsymbol{y}(\boldsymbol{x})$ is the deterministic model relating parameters and observations, that is, the forward-modeled gravity response from the given mass density distribution. Indeed, although $\boldsymbol{y}(\boldsymbol{x})$ is formally a function of both densities and labels, it depends on the densities only, while the labels enter indirectly through the prior probability.

The prior probability $P(\boldsymbol{x})$ is built to reflect the expectation on the spatial distribution of the model units and their physical properties. To this aim, we split the joint distribution of the full set of model parameters $x$ as:

$$P(\boldsymbol{x}) = \prod_{i=1}^{N} P(\rho_i|L_i)\, P(\boldsymbol{L}) \tag{3}$$

The conditional probability distribution of the density $\rho_i$ given the value of label $L_i$ for the corresponding voxel is modeled as a Gaussian:

**Table 2**
*A Priori Density Values per GUESS Unit, With 1σ Uncertainty*

| Unit | Description | Density (kg/m$^3$) | Reference |
|---|---|---|---|
| 1 | Quaternary volcanic rocks | 1,801 ± 42 | Pola et al. (2014) |
| 2 | Cenozoic terrigenous sediments | 2,325 ± 45 | Mancinelli et al. (2019)[a] |
| 3 | Mesozoic carbonates | 2,600 ± 58 | Mancinelli et al. (2019)[b] |
| 4 | Permian clastic units | 2,550 ± 77 | Mancinelli et al. (2019)[c] |
| 5 | Upper Crust | 2,800 ± 84 | Mancinelli et al. (2019)[c] |
| 6 | Lower Crust | 2,900 ± 87 | Mancinelli et al. (2019)[c] |

[a]Central value and 1$\sigma$ correspond, respectively, to the mean and one third of the range from Table 1 of Mancinelli et al. (2019) for "Holocene to upper Miocene turbiditic and continental deposits". [b]As (a) but for "Lower Miocene to Jurassic carbonatic and marly sequences and the Triassic unit." [c]No range is reported by Mancinelli et al. (2019) for this unit, and the 1$\sigma$ is set to 3% of the central value, above the 1.9%–2.2% of Units 2 and 3.

$$P(\rho_i | L_i) \propto \exp\left\{-\frac{[\rho - \mu_\rho(L_i)]^2}{2\sigma_\rho^2(L_i)}\right\} \tag{4}$$

where $\mu_\rho(L_i)$ and $\sigma_\rho^2(L_i)$ are the mean and the variance of the density for the considered label, respectively, as provided in Table 2. Meanwhile, the marginal probability distribution of the labels is described as a Markov Random Field, resulting in a Gibbs probability distribution (Azencott, 1988):

$$P(\boldsymbol{L}) \propto \exp\left\{-\frac{1}{2}\gamma\sum_{i=1}^{N} s_i^2(L_i) - \frac{1}{2}\lambda\sum_{i=1}^{N}\sum_{j\in\Delta_i} q^2(L_i, L_j)\right\} \tag{5}$$

The penalty functions are $s_i^2(L_i)$ and $q^2(L_i,L_j)$. The former penalizes label differences with respect to introduced in Section 2.3 , while the latter enforces homogeneity among labels in the neighborhood $\Delta_i$ of the considered voxel $i$, preferring models with smooth boundary surfaces between model units. The constants $\gamma$ and $\lambda$ weight the contribution of the two penalties in the posterior probability distribution. Further details about the algorithm are in Rossi et al. (2015), Rossi (2017), and Reguzzoni et al. (2019).

Combining the prior probability and the likelihood distributions (Equations 2–5) according to Equation 1, the posterior probability distribution is derived. Then introducing the Maximum A Posteriori principle, the solution is obtained by minimizing the following target function:

$$F(\boldsymbol{\rho},\boldsymbol{L}|\boldsymbol{y}^o) = [\boldsymbol{y}^o - \boldsymbol{y}(\boldsymbol{x})]^T \mathbf{C}_{\nu\nu}^{-1} [\boldsymbol{y}^o - \boldsymbol{y}(\boldsymbol{x})] + \sum_{i=1}^{N} \frac{[\rho - \mu_\rho(L_i)]^2}{\sigma_\rho^2(L_i)} + \gamma\sum_{i=1}^{N} s_i^2(L_i) + \lambda\sum_{i=1}^{N}\sum_{j\in\Delta_i} q^2(L_i, L_j) \tag{6}$$

The minimization is performed by a simulated annealing supported by a Gibbs sampler, which are capable of exploring complex, high-dimensional solution spaces while respecting hard constraints on density and geometry.

To prevent this minimization procedure from converging to formally optimal but physically unrealistic solutions, additional deterministic constraints are introduced in the optimization procedure, thus limiting the research space of possible solutions. As for the densities, their values are limited within a range of $\pm 3\sigma_\rho$ given the unit, and their spatial variability inside the same unit is controlled by setting thresholds on the allowed lateral and vertical density variations. As for the geometries, only some configurations of labels in the voxel neighborhood are admitted, for example, by introducing a constraint on the minimum number of voxels with the same label within the neighborhood. This enforces the information provided by the function $q^2$ (see Equation 5) to get smooth boundary surfaces between different model units.

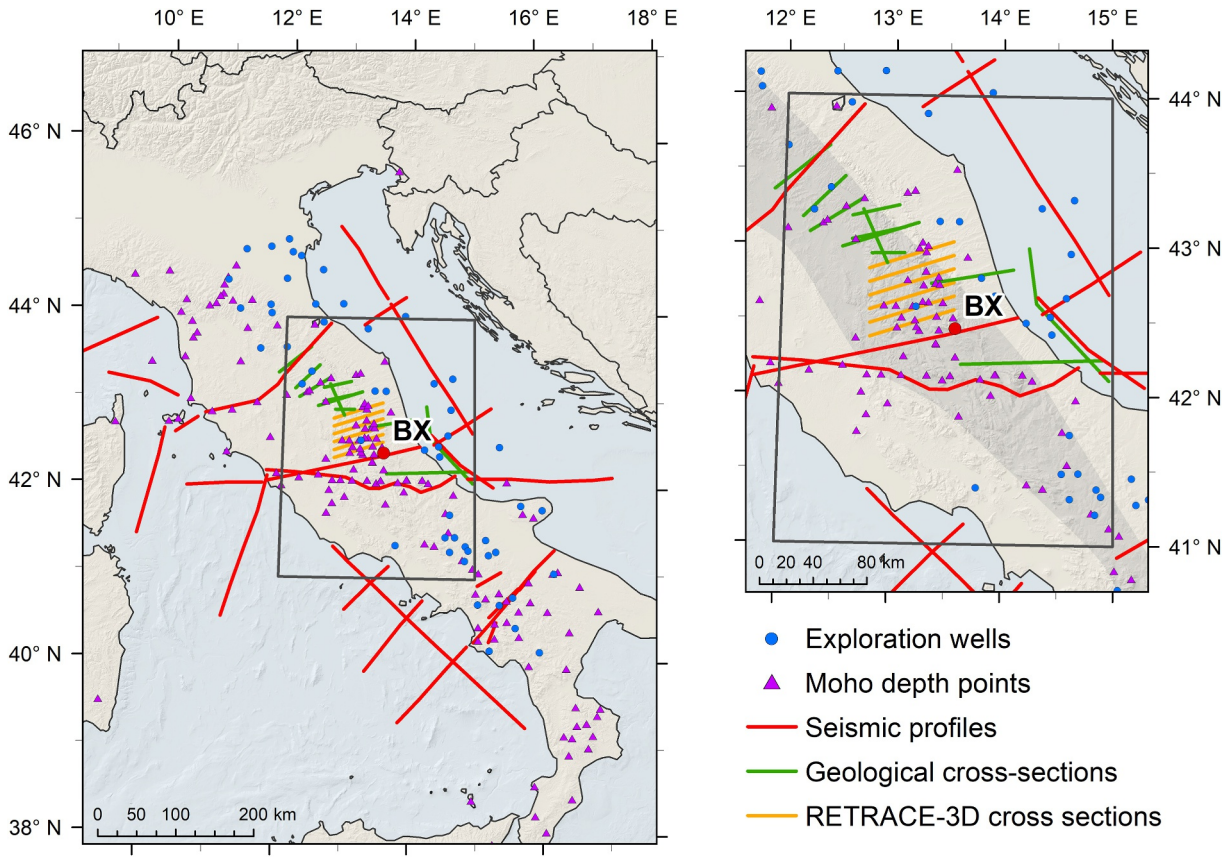



**Figure 2.** Spatial distribution of the inputs used to constrain the a priori crustal model: 53 ViDEPI exploration wells (blue dots), 154 Moho depth points (purple triangles), seismic-interpreted cross-sections (red), geological cross-sections (green), and RETRACE-3D cross-sections (yellow). The black box outlines the study area centered on Borexino (BX); the right panel zooms on the central tile, with the shaded Apennine-foreland transition zone where 40% uncertainty was assigned to Upper Crust, Lower Crust, and Moho interfaces.

### 2.3. Building a Priori Crustal Model

The 3-D crustal model is built on a regular voxel grid of $4 \times 4 \times 0.1$ km extending from sea level down to 50 km depth. The model spans a $5° \times 5°$ region, with the inversion analysis restricted to the central $3° \times 3°$ tile to avoid edge effects from the 1° border. The reference Digital Elevation Model combines TINITALY (Tarquini et al., 2023) for topography and EMODnet (EMODnet Bathymetry Consortium, 2024) for bathymetry, both resampled to 100 m. The geological map of Figure 1b classifies the GUESS unit at the surface, with contacts vertically projected down to elevation zero for gravity stripping (Section 2.4). Inputs are summarized in Table S1 in Supporting Information S1.

Subsurface geometry is constrained by three categories of data. Stratigraphic logs from the ViDEPI database (Assomineraria, 2025) yield 53 deep exploration wells (Figure 2) (total depth 4.0–7.8 km) within a $5° \times 5°$ area around Borexino. Geological formations were clustered into GUESS units; the resulting depth-to-contact data, treated with no uncertainty given the reliability of borehole observations, constrain Units 1, 2, and 3.

Boundary surfaces of the deeper units (4, 5, and 6) are constrained by 38 2-D cross-sections (Figure 2), combining geological interpretations (D'Ambrosio et al., 2021; Di Luzio et al., 2009; Mirabella et al., 2008, 2011; Scisciani et al., 2014) with seismic-interpreted profiles (Barchi et al., 1998; Feriozzi et al., 2024; Finetti, 2005; Scrocca et al., 2007). Six SW-NE cross-sections from the RETRACE-3D model (Buttinelli et al., 2021; Di Bucci et al., 2021) refine the central area down to 8–10 km depth. The Permian-Triassic succession (Unit 4) is set to a thickness of $2 \pm 2$ km, allowing $1\sigma$ variation between 0 and 4 km consistent with documented data (Scrocca et al., 2007).

The Moho discontinuity is constrained by the gridded map of Spada et al. (2013) at 2 km spacing, with 25% uncertainty incorporating the 15% error reported by the authors plus interpolation effects, complemented by 154 receiver-function estimates of Moho depth (Di Luzio et al., 2009; Mele & Sandvol, 2003; Mele et al., 2006; Piana Agostinetti & Amato, 2009; Piana Agostinetti et al., 2022) selected for individual uncertainty below 20%.

The Adria-Tyrrhenian discontinuity is derived from the Database of Individual Seismogenic Sources (DISS Working Group, 2025) for the Northern Apennines, merged with the leading thrust of the Apulia carbonates (Feriozzi et al., 2024; Nicolai & Gambini, 2007) in the central and southern sectors.

A $1\sigma$ uncertainty of 20% is assigned to all 2-D cross-sections, raised to 40% in the Apennine-foreland transition zone and on the Adria-Tyrrhenian discontinuity itself, where structural heterogeneity is largest. Admissible depth ranges per voxel are computed by interpolating each constraint on the horizontal grid, opening $2 \times 3\sigma$ intervals around each depth.

A priori densities are assigned per GUESS unit (Table 2). Unit 1 (Quaternary volcanics) takes the value reported for lavas and pyroclastic rocks of the Latium-Campania provinces (Pola et al., 2014). Units 2–6 follow the last column of Table 1 of Mancinelli et al. (2019), where literature, laboratory and well data are integrated within a joint gravity-magnetic framework, ensuring internal consistency across the stratigraphic sequence. The $1\sigma$ uncertainty for Units 2 and 3 is set to one third of the Mancinelli ranges for "Holocene to upper Miocene turbiditic and continental deposits" and "Lower Miocene to Jurassic carbonatic and marly sequences" respectively; for Units 4 ("Metamorphic Basement"), 5 ("Basement"), and 6 ("Lower Crust") a conservative 3% is adopted. Subsequent literature contributions (Montone & Mariucci, 2020, 2026; Tiberti et al., 2026), characterized by unit-specific density determinations over a subset of stratigraphic intervals, are discussed in Section 4 for an independent consistency assessment of the GUESS model. None of these estimates enters the prior. The sonic-log densities of Montone and Mariucci (2020, 2026), derived from well *P*-wave velocities, serve only as validation benchmarks.

### 2.4. Gravity Data

The gravity observations used in the inversion were obtained by gridding some ground gravity disturbances available for the study region (Barzaghi et al., 2007). The choice of producing a grid of data to be inverted, instead of using directly the original sparse data, was driven by the need of minimizing the computational burden of the forward modeling during the inversion procedure. In fact, given regular grids of voxels and observation points, the gravity forward modeling relationship acts as an integration kernel, allowing the application of the Fourier transform to speed up the computation. This also requires working in planar approximation and having observations at the same height.

To compute the observation grid, the collocation approach was adopted in the frame of a remove-compute-restore procedure (Barzaghi et al., 2007; Sansò & Sideris, 2012). The ground observations were reduced by the effects of the low frequencies of the gravity model and of the high frequencies mainly caused by the topographical masses. To implement this reduction, the gravity signal generated from XGM2019e (Zingerle et al., 2020) up to spherical harmonic degree and order 5540 was removed from the observations. This model combines gravity data (up to degree 719) and the effect of the topographical masses. The so-computed residual gravity disturbances $\boldsymbol{\delta g}^{o}_{\mathrm{res}}$ were gridded at a constant height by means of the collocation approach as (Moritz, 1980; Sansò & Sideris, 2012):

$$\widehat{\boldsymbol{\delta g}}^{\mathbf{grid}}_{\mathbf{res}} = \mathbf{C}_{\delta g^{\mathrm{grid}}_{\mathrm{res}} \delta g_{\mathrm{res}}} \left( \mathbf{C}_{\delta g_{\mathrm{res}} \delta g_{\mathrm{res}}} + \sigma_\eta^2 \mathbf{I} \right)^{-1} \boldsymbol{\delta g}^{o}_{\mathrm{res}} \tag{7}$$

where the covariance matrices $\mathbf{C}_{\delta g^{\mathrm{grid}}_{\mathrm{res}} \delta g_{\mathrm{res}}}$ and $\mathbf{C}_{\delta g_{\mathrm{res}} \delta g_{\mathrm{res}}}$ represent the stochastic behavior of the gravity signal and were evaluated by using a homogeneous and isotropic Gaussian covariance model, while $\sigma_\eta^2$ is the observation noise variance and I the identity matrix. The covariance model parameters together with noise variance are estimated by interpolating the empirical covariance function of the original data (Knudsen, 1987). Finally, the XGM2019e was restored to the $\widehat{\boldsymbol{\delta g}}^{\mathbf{grid}}_{\mathbf{res}}$ gridded residuals thus obtaining the $\boldsymbol{y}^{o}$ set of observations to be used in Equation 6, as well as their error variances obtained by formal covariance propagation through Equation 7. The grid was defined at a constant height of 3,000 m to be safely outside from the masses with the same resolution of

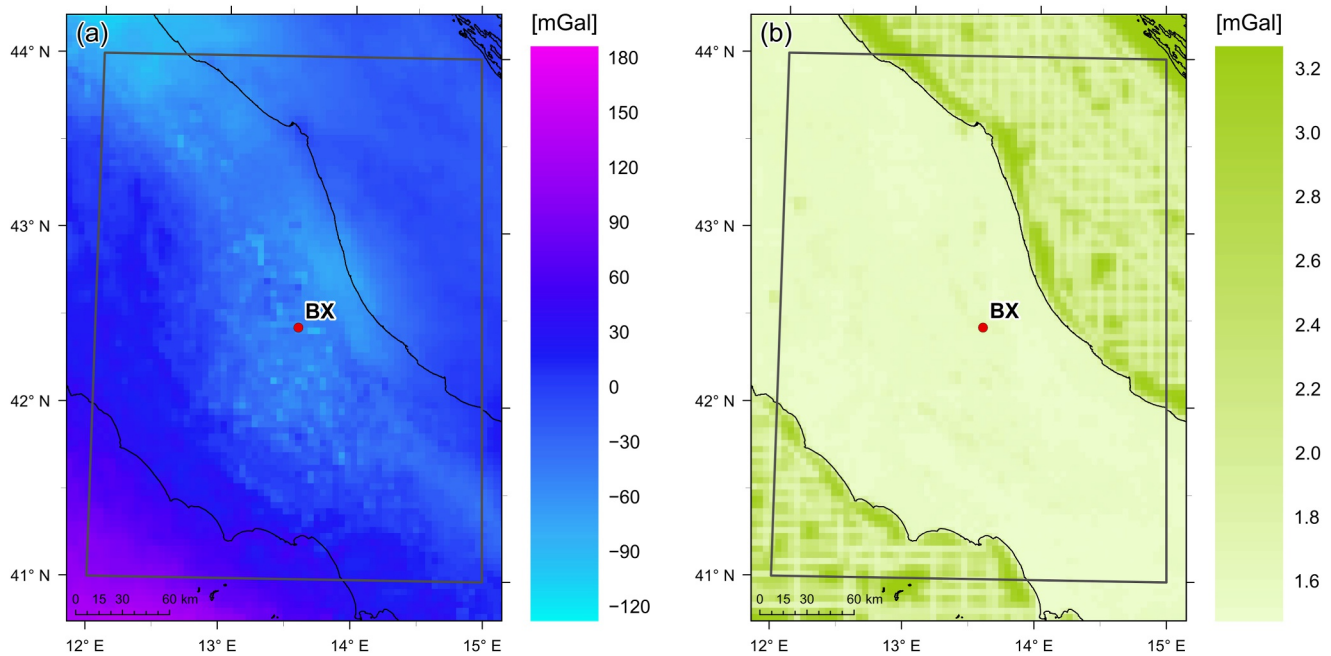



**Figure 3.** (a) Gridded gravity observations after stripping topography, bathymetry and deep-mantle contributions, used as input to the Bayesian inversion. (b) Standard deviation at each grid node, in mGal.

the voxel model (4 × 4 km) and was extended beyond the central tile region by a border of about 1° to reduce edge effects. The accuracy of the gridded data is in the order of few mGal standard deviation (Figure 3b).

To isolate the signal due to the mass volume under study, that is, from the 0-elevation level down to 50 km, the topographic, bathymetric, and deep-mantle contributions were computed and stripped from the data. As for the topography and bathymetry, their geometry was modeled according to the DEM presented in Section 2.3 at 100 m horizontal resolution, while their density was modeled according to the geological model of Figure 1b by introducing the mean density of each model unit from the Earth surface down (for topography) or up (for bathymetry) to the 0-elevation level. The gravity effect was computed with the GTE software (Capponi et al., 2018; Sampietro et al., 2016). The deep mantle effect was assumed to be equivalent to the signal of the XGM2019e global gravity model up to spherical harmonic degree and order of 12 (Tadiello & Braitenberg, 2021).

The gravity observation grid used as input for the inversion procedure is shown in Figure 3, together with its accuracy.

## 3. Results

### 3.1. Gravimetric Solution

The inverse gravimetric model was estimated through minimization of the target function in Equation 6. In this equation there are some parameters of the prior probability distribution that need to be empirically calibrated. These are the weights $\lambda$ and $\gamma$, the parameters of the penalty functions $s_i^2(L_i)$ and $q^2(L_i,L_j)$, and the thresholds controlling the deterministic constraints, for example, the maximum allowed lateral and vertical density variations and the minimum number of voxels with the same label within the neighborhood of each voxel. To properly span the solution space, the impact of these parameters is studied by selecting three significant values for each parameter and computing a gravimetric inversion for all their possible combinations. To this aim, an overall number of about 2,200 solutions was computed. Each solution required approximately 5 hr of computation, corresponding to about 2 days of processing when using multiple parallel jobs on a computer cluster equipped with approximately 250 cores and 1 TB of RAM overall.

Similarly to what was presented in Reguzzoni et al. (2019), the candidate models were ranked and the best solution selected. A direct evaluation of the target function values (Equation 6) would not have been meaningful

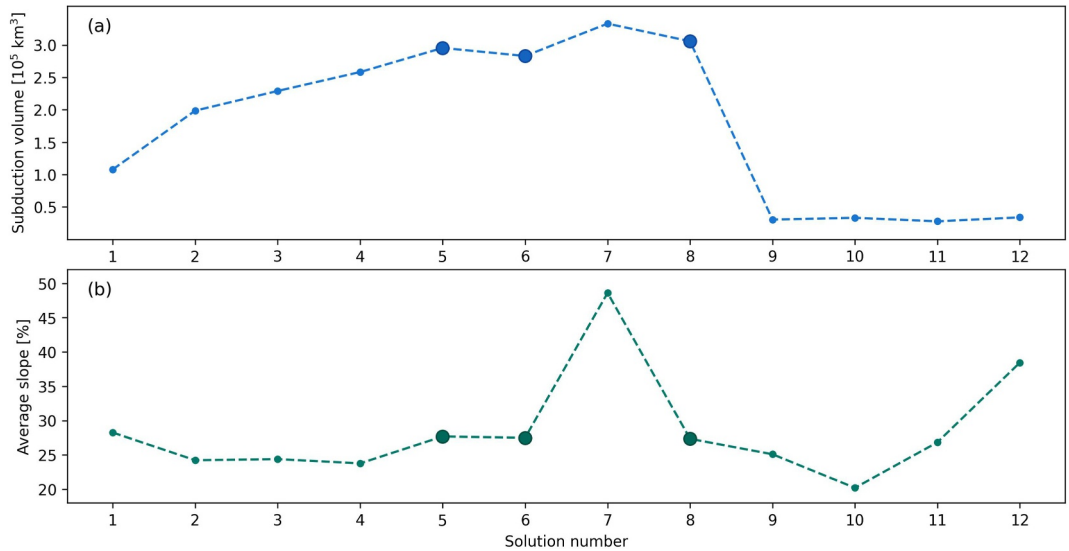



**Figure 4.** (a) Adria subduction volume and (b) average slope of unit boundary surfaces for the 12 cluster representatives. Solutions 5, 6, and 8 combine the largest subduction volume with the smoothest boundaries and were retained as effectively equivalent for the refinement set.

because of the missing normalization. Therefore, a set of indexes was calculated for each estimated solution to highlight and quantify relevant geological features of the models. The considered indexes are:

1. The gravity residuals over the central tile (standard deviation),
2. The volume of the voxels involved in the subduction zone,
3. The average slope of the boundary surfaces dividing the model units.

To find the best inverse gravimetric solution among the computed ones, the idea is to search for those (a) fitting the gravity data with a standard deviation better than 6 mGal, (b) including the largest possible subduction of the Adria plate below the Tyrrhenian one, (c) with the smoothest possible interfaces between different model units. These criteria are driven by (a) the accuracy of the gravity grid (Figure 3b), choosing the threshold of 6 mGal as twice the highest error standard deviation to account also for possible mismodeling in the terrain correction, (b) the expected geometry given the geological setting of the region and the consideration that the inversion algorithm tends to minimize the extent of the subduction, (c) the higher plausibility of smooth boundaries between geological units rather than rough surfaces.

Once the criteria were defined, we first excluded the solutions with a too large gravity fitting, then we grouped the remaining solutions into 12 clusters on the basis of their subduction volume; finally, for each of these clusters we chose the solution with the smoothest boundary surfaces (according to the average slope). The indexes describing the overall volume of the subduction and the average slope of the boundary surfaces for the selected 12 solutions are displayed in Figure 4.

With the aim of maximizing the subduction volume according to the geological expectations, but having the smoothest possible boundary surfaces, solutions 5, 6, and 8 result to be almost equivalent and, therefore, they are selected among the others. Given this finding, a further set of about 1,000 solutions (hereafter referred to as the refinement set) is computed to evaluate the impact of the input parameters that are different in the three optimal solutions with a finer discretization step. The final estimated inverse gravity model is obtained by combining these ∼1,000 refined solutions. For each voxel, the modal value of the labels is taken (Figures 6a, 7a, 8a, and 9a) while the mean value of the density is computed by considering only the solutions for which the label is equal to the chosen modal value. The final solution in terms of labels and densities led to a fit of the observed gravity field with a residual standard deviation of about 5.7 mGal, improving the fit of the a priori geological model by a factor 10 (Figure 5).

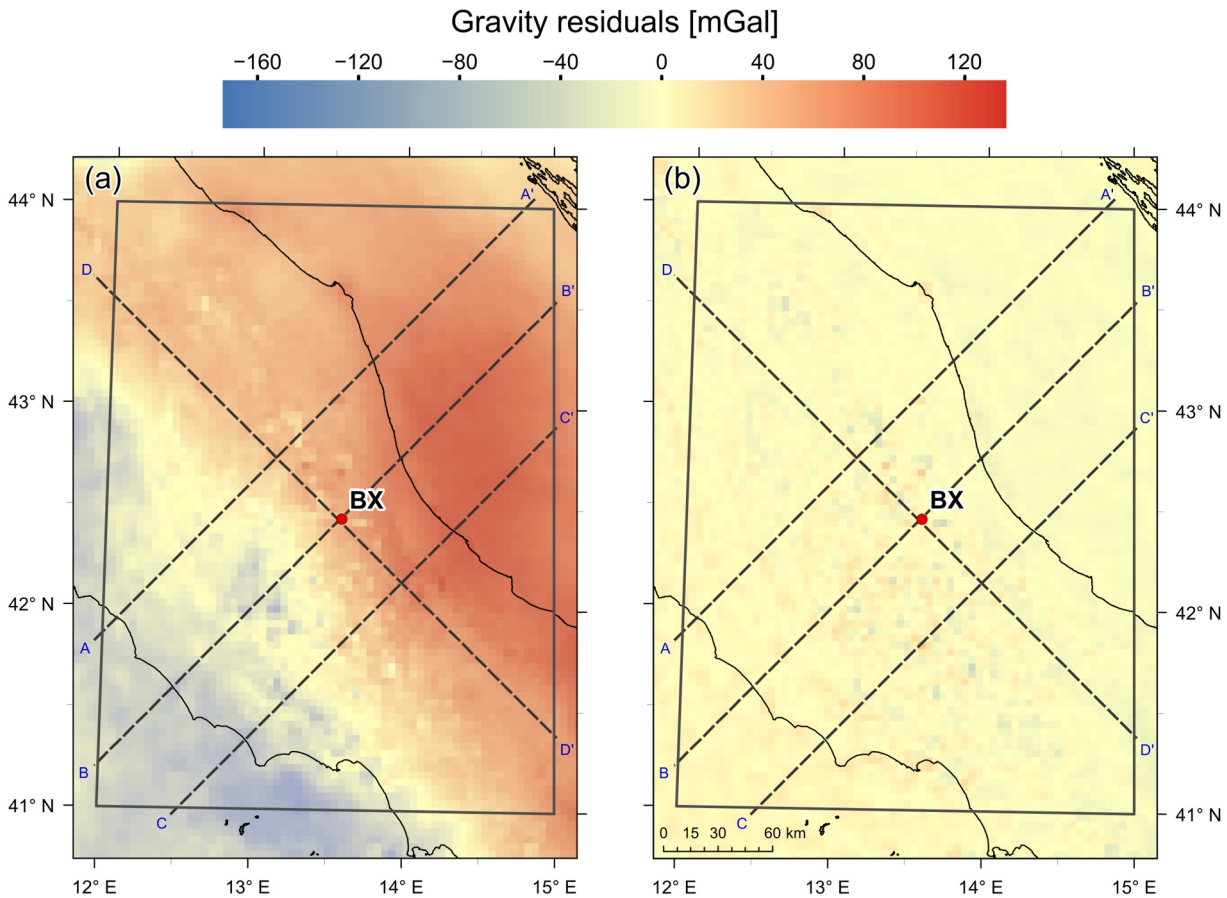



**Figure 5.** Gravity residuals of (a) the a priori crustal model and (b) the final estimated GUESS model. The order-of-magnitude reduction in residual standard deviation (final misfit 5.7 mGal) reflects the data fusion enabled by the Bayesian inversion. Traces of cross-sections AA' to DD' are overlaid.

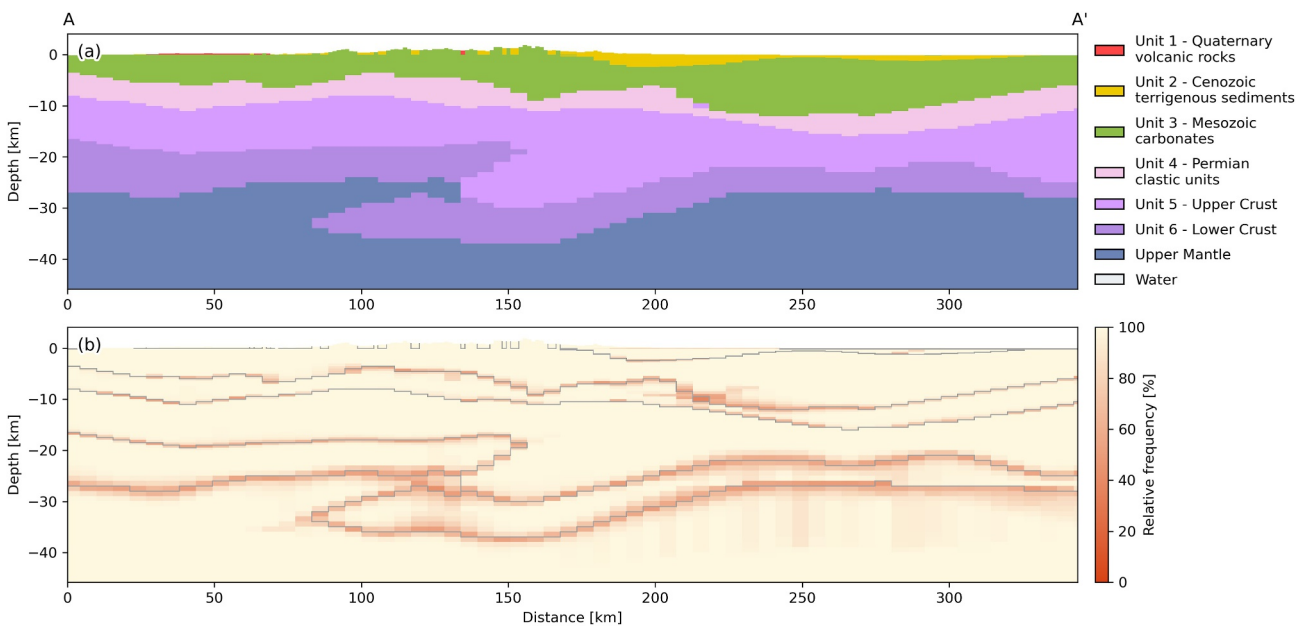



**Figure 6.** Virtual cross-section AA' (traced in Figure 5): (a) GUESS unit geometry, (b) voxel-wise relative frequency of the modal label across the 1,000 refinement inversions, quantifying geometric uncertainty. The gray lines in panel (b) highlight the boundaries between adjacent GUESS units as shown in panel (a).

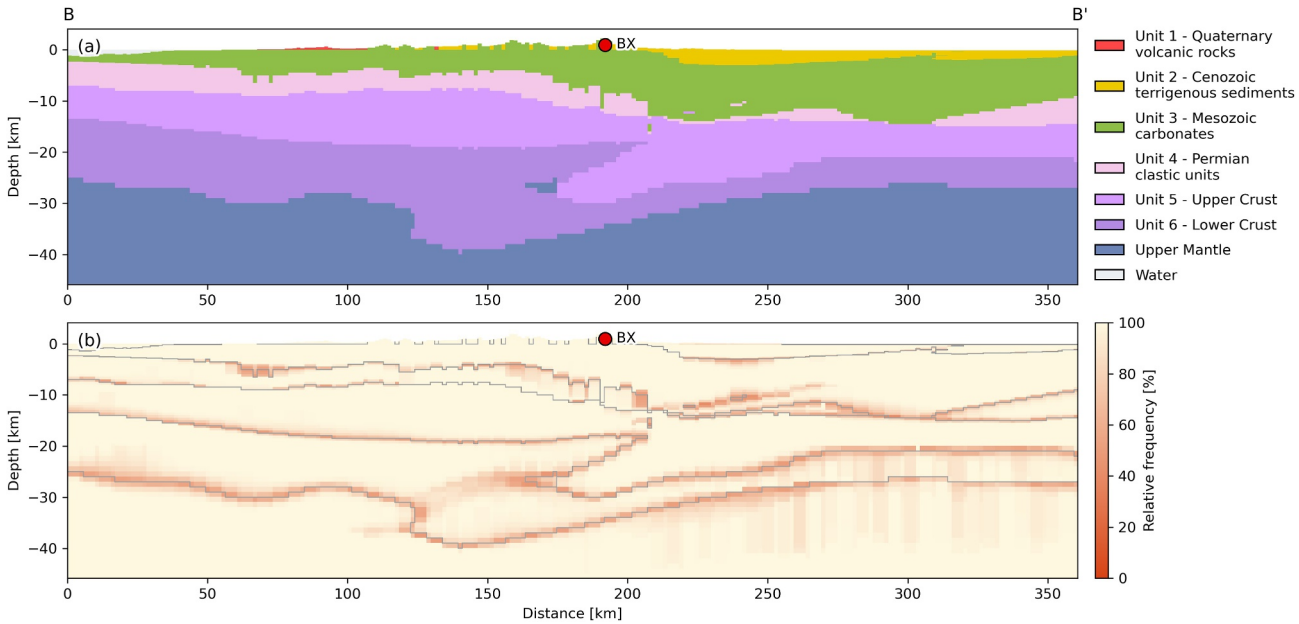



**Figure 7.** Virtual cross-section BB' (traced in Figure 5): (a) GUESS unit geometry, (b) voxel-wise relative frequency of the modal label across the 1,000 refinement inversions, quantifying geometric uncertainty. The gray lines in panel (b) highlight the boundaries between adjacent GUESS units as shown in panel (a).

The overall mass and volume of each model unit, as well as their average density in the final solution, are presented in Table 3. The estimation accuracies of masses and volumes are computed by evaluating the empirical standard deviation of the 1,000 solutions of the refinement set (Table 3).

Finally, the estimation accuracy of the geometry is computed voxel-wise, by evaluating the relative frequency of each label for each voxel. Since the most frequent labels are the ones constituting the final model, the corresponding relative frequencies for each voxel are presented in Figures 6b, 7b, 8b, and 9b.

### 3.2. Geoneutrino Signals

The geoneutrino signal at the Borexino location is computed by integrating the contribution of every voxel within the GUESS volume, weighted by the U or Th abundance, the rock density, the Inverse Beta Decay (IBD) cross-section, the three-flavor electron antineutrino survival probability and the $1/r^2$ geometric flux dilution (Bellini et al., 2021; Fiorentini et al., 2007):

$$S(X,\vec{r}) = N_p \cdot T \cdot \varepsilon_{\bar{\nu}_e} \cdot \eta \cdot \int dE_{\bar{\nu}} \cdot \sigma(E_{\bar{\nu}}) \cdot S_p(X,E_{\bar{\nu}}) \cdot \int d^3r' \cdot P_{ee}(|\boldsymbol{r}-\boldsymbol{r}'|,E_{\bar{\nu}}) \cdot \frac{a(X,\boldsymbol{r}') \cdot \rho(\boldsymbol{r}')}{4\pi|\boldsymbol{r}-\boldsymbol{r}'|^2} \quad (8)$$

**Table 3**
*Per-Unit Volume, Mass, Average Density, and Unitary Geoneutrino Signals G(U) and G(Th) of the GUESS Model*

| Unit | Description | Volume ($10^3$ km$^3$) | Volume (%) | Mass ($10^{15}$ kg) | Mass (%) | Average density (kg/m$^3$) | G(U) (TNU) | G(Th) (TNU) |
|---|---|---|---|---|---|---|---|---|
| 1 | Quaternary volcanics | 1.2 | 0.05 | 2.2 | 0.03 | 1,801 | $7.22 \times 10^{-4}$ | $4.89 \times 10^{-5}$ |
| 2 | Cenozoic terrigenous sediments | 55.8 ± 1.4 | 2.3 | 130.2 ± 3.3 | 1.9 | 2,332 ± 83 | 0.17 ± 0.01 | 0.012 ± 0.001 |
| 3 | Mesozoic carbonates | 585.1 ± 3.9 | 23.8 | 1,533.8 ± 10.5 | 22.6 | 2,621 ± 25 | 2.93 ± 0.02 | 0.201 ± 0.001 |
| 4 | Permian clastic units | 285.1 ± 4.9 | 11.6 | 724.0 ± 12.6 | 10.7 | 2,539 ± 62 | 0.49 ± 0.02 | 0.034 ± 0.001 |
| 5 | Upper Crust | 795.7 ± 8.2 | 32.3 | 2,244.7 ± 23.4 | 33.1 | 2,821 ± 41 | 1.36 ± 0.02 | 0.095 ± 0.001 |
| 6 | Lower Crust | 737.0 ± 15.3 | 30.0 | 2,150.2 ± 45.4 | 31.7 | 2,918 ± 86 | 1.20 ± 0.03 | 0.086 ± 0.001 |

*Note.* Volume and mass uncertainties are the empirical standard deviation across the 1,000 refinement inversions; density uncertainty is propagated assuming statistical independence. G(U) and G(Th) are computed for unitary abundances (aU = aTh = 1 μg/g) and act as scaling factors: the actual geoneutrino signal of each unit is recovered by multiplying G by the realistic U and Th content. Reported uncertainties on G quantify the structural (geometry-and-density) contribution only.

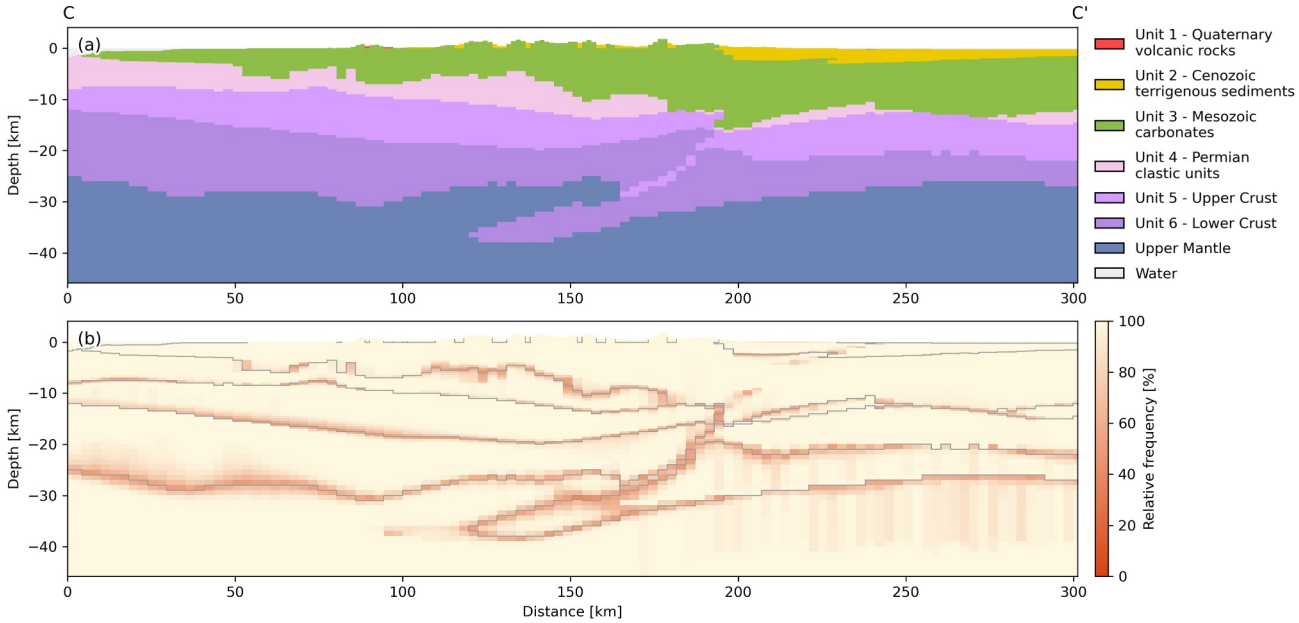



**Figure 8.** Virtual cross-section CC' (traced in Figure 5): (a) GUESS unit geometry, (b) voxel-wise relative frequency of the modal label across the 1,000 refinement inversions, quantifying geometric uncertainty. The gray lines in panel (b) highlight the boundaries between adjacent GUESS units as shown in panel (a).

where the integral runs over the GUESS volume.

The IBD cross-section follows the formulation of Strumia and Vissani (2003), which includes radiative corrections and threshold effects relevant at geoneutrino energies. The electron antineutrino survival probability uses the three-flavor vacuum formalism of Capozzi et al. (2014, Equation 37) with the latest oscillation parameters ($\sin^2\theta_{12}$, $\sin^2\theta_{13}$, $\delta m^2$, $\Delta m^2$) from the Particle Data Group (Navas et al., 2024; Particle Data Group, 2025). Geoneutrino signals are expressed in Terrestrial Neutrino Units (TNU): one TNU corresponds to one IBD event per year in a detector with $10^{32}$ free protons under perfect efficiency.

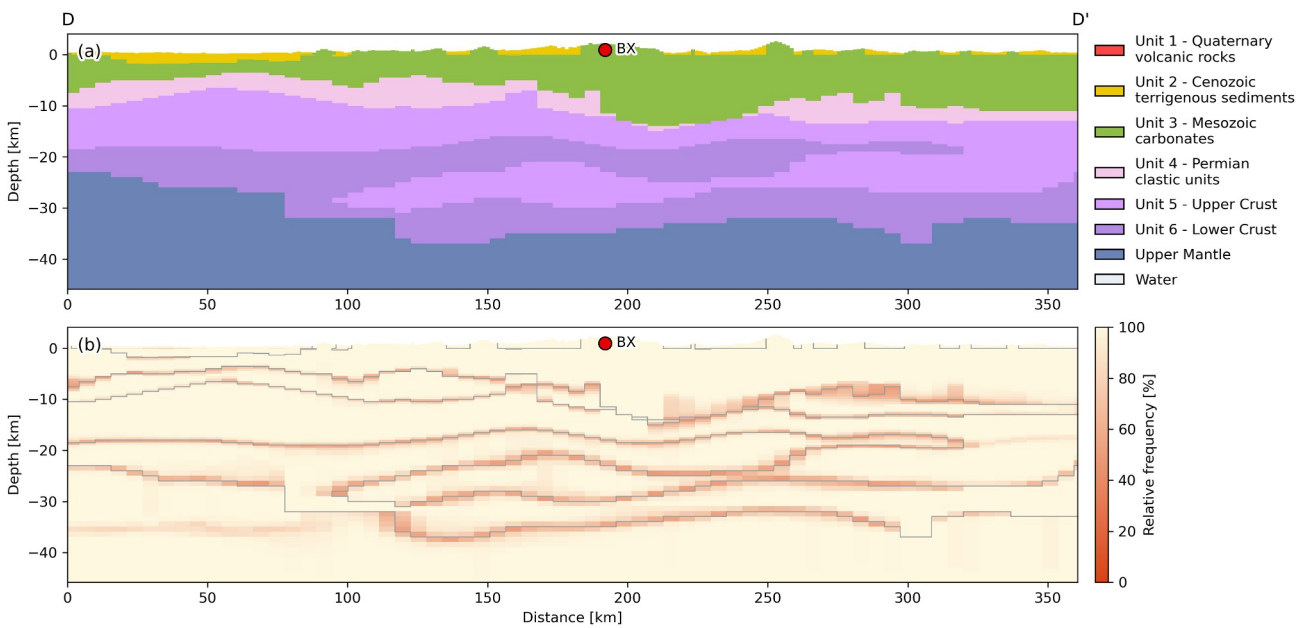



**Figure 9.** Virtual cross-section DD' (traced in Figure 5): (a) GUESS unit geometry, (b) voxel-wise relative frequency of the modal label across the 1,000 refinement inversions, quantifying geometric uncertainty. The gray lines in panel (b) highlight the boundaries between adjacent GUESS units as shown in panel (a).

For the flux integration, the GUESS voxel grid is locally refined to $0.1 \times 0.1 \times 0.1$ km. Each refined voxel inherits the GUESS unit label and the corresponding posterior density and is assigned unitary U and Th abundances (aU = 1 μg/g and aTh = 1 μg/g). The integral over the volume of each unit yields G(U) and G(Th) per unit (Table 3), expressed in TNU per μg/g of crustal abundance. These unitary signals are scaling factors: the actual geoneutrino signal of each unit is recovered by multiplying G(U) and G(Th) by the realistic U and Th abundances of that unit. This separation isolates the geophysical contribution to the predicted signal from the geochemical (i.e., U and Th) variability, which is treated separately and is the subject of follow-up work.

The structural uncertainty on the predicted signal is propagated by repeating the calculation over each of the 1,000 refinement inversions of Section 3.1, building the distribution of G(U) and G(Th) per unit. The reported uncertainty (Table 3) is the standard deviation of this distribution and quantifies only the geometry-and-density contribution; the residual geochemical uncertainty associated with U and Th abundances is not included and represents the dominant remaining error budget for the absolute crustal signal.

## 4. Discussion

The interpretation of Borexino geoneutrino measurements requires a local crustal model whose precision matches the experimental uncertainty. GUESS replaces the deterministic reference of Coltorti et al. (2011) with a probabilistic 3-D model in which every GUESS unit carries a quantified mass-and-volume uncertainty derived from the gravity inversion. The Bayesian integration of multi-source data, including teleseismic receiver functions, deep wells, seismic reflection cross-sections, satellite gravity and high-resolution topography, treats the local crustal contribution as a posterior distribution rather than a single value, enabling a more reliable separation of the mantle component in the multi-site geoneutrino analysis.

The 2,200 candidate inversions used during calibration sample the prior space densely enough that the selected solution is unlikely to be a local minimum of the target function. The final gravity misfit of 5.7 mGal is consistent with the observation accuracy and improves the a priori model fit by an order of magnitude, confirming that the Bayesian fusion of geophysical constraints captures the dominant features of the subsurface mass distribution. The 1,000 refinement inversions further provide a first-order estimate of the structural variability and ensure that the inferred geometry is not an artifact of a particular parameter choice.

The crystalline crust (Units 5 and 6) accounts for 62.3% of the total volume and 64.8% of the total mass, with the largest absolute uncertainties on the LC (2.1% relative on both volume and mass) reflecting the limited direct seismic constraint at depth and the geodynamic complexity of the Adria subduction. The Mesozoic carbonates (Unit 3) form a well-constrained reservoir with 23.8% volume fraction and 0.7% relative uncertainty, consistent with the structural homogeneity of the Apennine carbonate platform. The Quaternary volcanics (Unit 1) contribute only 0.03% of the total mass but are tracked separately because their high U and Th content makes them disproportionately important for the geoneutrino signal.

Comparing GUESS with Coltorti et al. (2011) on the common $2° \times 2°$ central tile (Figure 10) reveals a substantial internal redistribution of mass with nearly invariant totals: total volume and mass differ by 0.06% and 0.01% respectively. Unit 2 (Cenozoic terrigenous) decreases to about 65% of its volume and mass, while Unit 4 (Permian-Triassic) grows by approximately a factor of four in both. The combined contribution of Units 5 and 6 is essentially unchanged, indicating that the redistribution is between Unit 2 and Unit 4 with the underlying UC acting as a buffer. The methodological cause is direct: Coltorti et al. (2011) prescribed a uniform 700 m thickness for the Permian-Triassic succession, while GUESS introduces a $2 \pm 2$ km a priori thickness (Section 2.3) that is then refined by the Bayesian inversion under the gravity constraint. The redistribution has direct consequences on the spatial attribution of radiogenic sources and therefore on the predicted crustal geoneutrino signal.

Density variability across units mirrors the underlying geological heterogeneity (Table 3). Unit 2 shows the largest relative dispersion (3.6%, $2{,}332 \pm 83$ kg/m$^3$), in agreement with the broad range of grain size, porosity and compaction expected for Cenozoic terrigenous successions. Unit 3 is markedly more stable (1.0%, $2{,}621 \pm 25$ kg/m$^3$) reflecting the lithological continuity of the Mesozoic carbonate domain, and Unit 4 shows an intermediate variability (2.4%, $2{,}539 \pm 62$ kg/m$^3$) consistent with its mixed composition.

Posterior densities are validated against three independent data sets through a normalized deviation $Z$ (the ratio between central-value differences and quadrature-combined uncertainties). Unit-aggregated densities from Figure 7b of Montone and Mariucci (2020) yield $|Z| < 2$ for Units 2, 3, and 4. Figure 3 estimates of Tiberti et al. (2026) yield

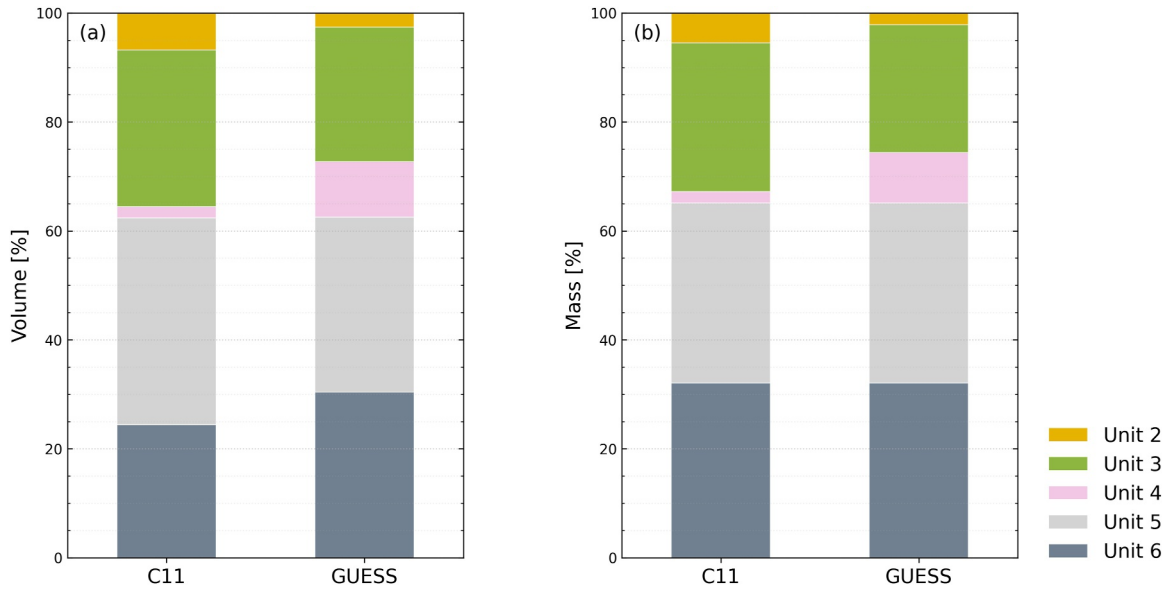



**Figure 10.** Relative distribution of GUESS units in the present model and in the Coltorti et al. (2011, C11) reference, as (a) percentage of total volume and (b) total mass over the common 2° × 2° tile. Unit 1 is omitted (0.03% volume, 0.02% mass in GUESS within the 2° × 2° tile, absent in C11).

$|Z| < 2$ for Units 2 and 3 (the only units the comparison covers). Sampling the GUESS posterior at the 18 well locations of Montone and Mariucci (2026) and aggregating per unit yields mean values of 2,329 ± 18 kg/m$^3$ for Unit 2 and 2,629 ± 28 kg/m$^3$ for Unit 3, against sonic-log compilations of 2,375 ± 72 and 2,669 ± 87 kg/m$^3$. The corresponding average relative misfits are 1.9% and 1.5%, again with $|Z| < 2$. The agreement on three independent benchmarks confirms that the Bayesian inversion drives the model toward in situ-consistent densities despite the use of generalized literature priors. Per-unit benchmark ranges are visualized in Figure 11. Detailed *Z*-score formulas and per-well comparison results are reported in Text S2 in Supporting Information S1.

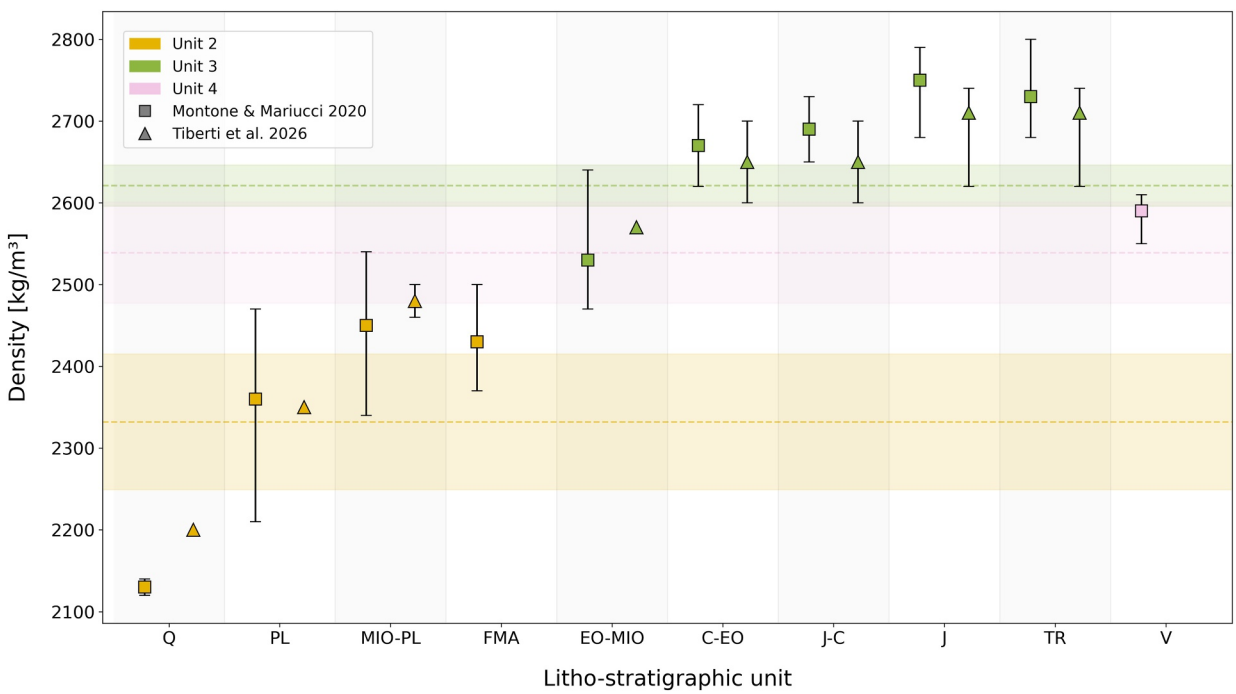



**Figure 11.** Independent density benchmarks for GUESS Units 2, 3, and 4. Squares: per-unit values from Figure 7b of Montone and Mariucci (2020). Triangles: values from Figure 3 of Tiberti et al. (2026). Horizontal bands: GUESS posterior mean ±1$\sigma$ per unit.

The GUESS framework follows the methodological precedents established for JUNO (Reguzzoni et al., 2019) and KamLAND (Takeuchi et al., 2019), confirming that probabilistic gravimetric inversion is now the standard tool for geoneutrino crustal modeling. Within the GUESS uncertainty budget, the structural-and-density contribution to the predicted signal is constrained to 1%–3% for the major units, an order of magnitude below the 20%–50% uncertainty typical of geochemical U and Th abundances. This shifts the dominant source of error in the absolute crustal geoneutrino prediction from crustal geometry to U and Th content, redirecting the next research priority toward the spatial distribution of HPEs.

Three limitations should be stated explicitly. The 4 km horizontal resolution is appropriate for regional gravity inversion but cannot resolve fine-scale structural details, which may affect mass estimates in marginal areas. In geodynamically complex sectors such as the Adria-Tyrrhenian transition zone, where direct seismic constraints are sparse, the Bayesian inversion retains a residual uncertainty on the lithological labels. The clustering of sedimentary units into broad geochemical categories (Units 2 and 3) ignores localized U and Th variations within each unit; the propagated density uncertainty is wide enough to cover the lithological range, but absolute U and Th estimates per unit will require dedicated geochemical sampling. For the crystalline crust, lithology-specific data such as those measured in the Adria-derived lower crust of the Ivrea-Verbano Zone (Lemke et al., 2026) could replace unit-average U and Th abundances in the next generation of the model.

## 5. Conclusions

The GUESS model establishes a new high-resolution 3-D reference for the Borexino local geoneutrino signal, substantially expanding the geophysical inputs of the previous reference of Coltorti et al. (2011). The Bayesian gravimetric inversion of multi-source data, including satellite gravity, high-resolution topography, deep wells, seismic profiles and receiver-function Moho constraints, achieves a gravity fit of 5.7 mGal that improves the a priori model by an order of magnitude. The voxel-wise output assigns density and lithological labels through Gibbs sampling with simulated annealing, propagating geometry and density uncertainties to a 1%–3% structural contribution to the predicted geoneutrino signal for the major units.

Posterior densities are statistically consistent with independent sonic-log compilations at 18 well locations and with regional 2-D density models, validating the probabilistic refinement against in situ data. The internal mass redistribution with respect to the previous reference, mass-conservative on the totals but substantial on individual units, propagates directly to the spatial attribution of radiogenic sources.

**Acknowledgments**
We are grateful to the Borexino Collaboration, which has always been close to and attentive to the geological questions raised by its measurements. The authors thank Gianpaolo Bellini, Eligio Lisi, Livia Ludhova, Gioacchino Ranucci, Barbara Ricci, and Andrea Serafini for useful discussions. We thank the anonymous reviewer for the constructive comments that improved the manuscript. This publication is based upon work from COST Action FuSe, CA24101, supported by COST (European Cooperation in Science and Technology). The work was carried out in the framework of the Agreement between the Centro di Geotecnologie (CGT), Dipartimento di Scienze Fisiche, della Terra e dell'Ambiente (DSFTA) of Siena University and the Istituto Nazionale di Geofisica e Vulcanologia (INGV), and benefited from the expertise and infrastructure of the Sismolab-3D (https://sismolab3d.ingv.it). The authors acknowledge the support of the University of Ferrara (Fondo di Ateneo per la Ricerca scientifica FAR 2023 and FAR 2024). *Funding*: This work is funded by project GUESS (GeoneUtrinos: mESSengers of the Earth's interior) funded by European Union – NextGenerationEU, Missione 4, Componente 1 (CUP: F53D23001280006).

## Conflict of Interest

The authors declare no conflicts of interest relevant to this study.

## Availability Statement

The stratigraphic well data used to constrain the a priori crustal model are available through the ViDEPI database (Assomineraria, 2025). The 2-D geological cross-sections are derived from published literature (Barchi et al., 1998; Buttinelli et al., 2021; D'Ambrosio et al., 2021; Di Bucci et al., 2021; Di Luzio et al., 2009; Feriozzi et al., 2024; Finetti, 2005; Mirabella et al., 2008, 2011; Scisciani et al., 2014; Scrocca et al., 2007). Moho depth constraints are from published sources (Di Luzio et al., 2009; Mele & Sandvol, 2003; Mele et al., 2006; Piana Agostinetti & Amato, 2009; Piana Agostinetti et al., 2022; Spada et al., 2013). The Adria–Tyrrhenian lithospheric discontinuity is derived from the Database of Individual Seismogenic Sources (DISS Working Group, 2025). The topographic surface is from the TINITALY Digital Elevation Model (Tarquini et al., 2023). Bathymetric data are from the EMODnet Digital Bathymetry (EMODnet Bathymetry Consortium, 2024). The density data used for model validation are from Montone and Mariucci (2026).

## References

Abusleme, A., Adam, T., Ahmad, S., Ahmed, R., Aiello, S., Akram, M., et al. (2022). JUNO physics and detector. *Progress in particle and nuclear Physics*, *123*, 103927. https://doi.org/10.1016/j.ppnp.2021.103927

Agostini, M., Altenmüller, K., Appel, S., Atroshchenko, V., Bagdasarian, Z., Basilico, D., et al. (2020). Comprehensive geoneutrino analysis with Borexino. *Physical Review D*, *101*(1), 012009. https://doi.org/10.1103/PhysRevD.101.012009

Allega, A., Anderson, M. R., Andringa, S., Askins, M., Asner, D. M., Auty, D. J., et al. (2025). Initial measurement of reactor antineutrino oscillation at SNO+. *European Physical Journal C*, *85*(1), 17. https://doi.org/10.1140/epjc/s10052-024-13687-5

Araki, T., Enomoto, S., Furuno, K., Gando, Y., Ichimura, K., Ikeda, H., et al. (2005). Experimental investigation of geologically produced antineutrinos with KamLAND. *Nature*, *436*(7050), 499–503. https://doi.org/10.1038/nature03980

Assomineraria. (2025). Progetto ViDEPI - Visibilità dei dati afferenti all'attività di esplorazione petrolifera in Italia [Dataset]. *Ministero dell'Ambiente e della Sicurezza Energetica - Direzione Generale Infrastrutture e Sicurezza Sistemi Energetici e Geominerari*. Retrieved from https://www.videpi.com

Azencott, R. (1988). Simulated annealing. *Séminaires de Mathématiques Supérieures*, *30*, 223–237.

Barchi, M., Minelli, G., & Pialli, G. (1998). The CROP 03 profile: A synthesis of results on deep structures of the Northern Apennines. *Memorie della Societa Geologica Italiana*, *52*, 383–400.

Barzaghi, R., Borghi, A., Carrion, D., & Sona, G. (2007). Refining the estimate of the Italian quasi-geoid. *Bollettino di Geodesia e Scienze Affini*, *3*, 145–160.

Bellini, G. (2024). Technological novelties and scientific discoveries with the Borexino experiment. *Annual Review of Nuclear and Particle Science*, *74*, 369–388. https://doi.org/10.1146/annurev-nucl-102622-021701

Bellini, G., Benziger, J., Bonetti, S., Avanzini, M. B., Caccianiga, B., Cadonati, L., et al. (2010). Observation of geo-neutrinos. *Physics Letters B*, *687*(4–5), 299–304. https://doi.org/10.1016/j.physletb.2010.03.051

Bellini, G., Inoue, K., Mantovani, F., Serafini, A., Strati, V., & Watanabe, H. (2021). Geoneutrinos and geoscience: An intriguing joint-venture. *La Rivista del Nuovo Cimento*, *45*, 1–105. https://doi.org/10.1007/s40766-021-00026-7

Bigi, G., Castellani, A., Catalano, R., Coli, M., Cosentino, D., Dal Piaz, G. V., et al. (1991). Synthetic structural-kinematic map of Italy, scale 1: 2,000,000. CNR Progetto Finalizzato Geodinamica - Structural model of Italy. S.E.L.C.A., Firenze.

Box, G. E. P., & Tiao, G. C. (1992). *Bayesian inference in statistical analysis*. Wiley.

Buttinelli, M., Petracchini, L., Maesano, F. E., D'Ambrogi, C., Scrocca, D., Marino, M., et al. (2021). The impact of structural complexity, fault segmentation, and reactivation on seismotectonics: Constraints from the upper crust of the 2016-2017 Central Italy seismic sequence area. *Tectonophysics*, *810*, 228861. https://doi.org/10.1016/j.tecto.2021.228861

Capozzi, F., Lisi, E., & Marrone, A. (2014). Neutrino mass hierarchy and electron neutrino oscillation parameters with one hundred thousand reactor events. *Physical Review D*, *89*(1), 013001. https://doi.org/10.1103/PhysRevD.89.013001

Capponi, M., Mansi, A. H., & Sampietro, D. (2018). Improving the computation of the gravitational terrain effect close to ground stations in the GTE software. *Studia Geophysica et Geodaetica*, *62*(2), 206–222. https://doi.org/10.1007/s11200-017-0814-3

Capuano, P., De Luca, G., Di Sena, F., Gasparini, P., & Scarpa, R. (1998). The density of the rock covering Gran Sasso Laboratories in Central Apennines, Italy by underground gravity measurements. *Journal of Applied Geophysics*, *39*(1), 25–33. https://doi.org/10.1016/s0926-9851(98)00002-0

Cassinis, R., Scarascia, S., & Lozej, A. (2003). The deep crustal structure of Italy and surrounding areas from seismic refraction data; a new synthesis. *Bollettino della Societa Geologica Italiana*, *122*, 365–376.

Coltorti, M., Boraso, R., Mantovani, F., Morsilli, M., Fiorentini, G., Riva, A., et al. (2011). U and Th content in the Central Apennines continental crust: A contribution to the determination of the geo-neutrinos flux at LNGS. *Geochimica et Cosmochimica Acta*, *75*(9), 2271–2294. https://doi.org/10.1016/j.gca.2011.01.024

Conti, P., Cornamusini, G., & Carmignani, L. (2020). An outline of the geology of the Northern Apennines (Italy), with geological map at 1: 250,000 scale. *Italian Journal of Geosciences*, *139*(2), 149–194. https://doi.org/10.3301/IJG.2019.25

D'Ambrosio, A., Lipparini, L., Bigi, S., Cassola, T., Bambridge, V. R., Derks, J. F., & Trippetta, F. (2021). Structural restoration and basin modelling of the Central Apennine orogen/foredeep/foreland system: New insights on the regional petroleum system. *Marine and Petroleum Geology*, *127*, 104977. https://doi.org/10.1016/j.marpetgeo.2021.104977

Di Bucci, D., Buttinelli, M., D'Ambrogi, C., Scrocca, D., Anzidei, M., Basili, R., et al. (2021). RETRACE-3D project: A multidisciplinary collaboration to build a crustal model for the 2016-2018 Central Italy seismic sequence. *Bulletin of Geophysics and Oceanography*, *62*(1), 1–18. https://doi.org/10.4430/bgta0343

Di Luzio, E., Mele, G., Tiberti, M. M., Cavinato, G. P., & Parotto, M. (2009). Moho deepening and shallow upper crustal delamination beneath the central Apennines. *Earth and Planetary Science Letters*, *280*(1–4), 1–12. https://doi.org/10.1016/j.epsl.2008.09.018

DISS Working Group. (2025). Database of individual seismogenic sources (DISS), version 3.3.1: A compilation of potential sources for earthquakes larger than M 5.5 in Italy and surrounding areas [Dataset]. *Istituto Nazionale di Geofisica e Vulcanologia (INGV)*. Retrieved from https://diss.ingv.it

Di Stefano, R., Bianchi, I., Ciaccio, M. G., Carrara, G., & Kissling, E. (2011). Three-dimensional Moho topography in Italy: New constraints from receiver functions and controlled source seismology. *Geochemistry, Geophysics, Geosystems*, *12*(9), Q09006. https://doi.org/10.1029/2011GC003649

EMODnet Bathymetry Consortium. (2024). EMODnet digital bathymetry (DTM 2024) [Dataset]. https://doi.org/10.12770/cf51df64-56f9-4a99-b1aa-36b8d7b743a1

Enomoto, S., Ohtani, E., Inoue, K., & Suzuki, A. (2007). Neutrino geophysics with KamLAND and future prospects. *Earth and Planetary Science Letters*, *258*(1–2), 147–159. https://doi.org/10.1016/j.epsl.2007.03.038

Feriozzi, F., Improta, L., Maesano, F. E., De Gori, P., & Basili, R. (2024). The 3D crustal structure in the epicentral region of the 1980, Mw 6.9, Southern Apennines earthquake (southern Italy). *Tectonics*, *43*, e2024TC008265. https://doi.org/10.1029/2024TC008265

Finetti, I. R. (Ed.) (2005). CROP project: Deep seismic exploration of the central Mediterranean and Italy. In *Atlases in geoscience 1*. Elsevier.

Finetti, I. R., Boccaletti, M., Bonini, M., Del Ben, A., Geletti, R., Pipan, M., & Sani, F. (2001). Crustal section based on CROP seismic data across the North Tyrrhenian-Northern Apennines-Adriatic Sea. *Tectonophysics*, *343*(3–4), 135–163. https://doi.org/10.1016/S0040-1951(01)00141-X

Fiorentini, G., Lissia, M., & Mantovani, F. (2007). Geo-neutrinos and Earth's interior. *Physics Reports*, *453*(5–6), 117–172. https://doi.org/10.1016/j.physrep.2007.09.001

Gao, R., Li, Z., Han, R., Wang, A., Li, Y., Xi, Y., et al. (2020). JULOC: A local 3-D high-resolution crustal model in South China for forecasting geoneutrino measurements at JUNO. *Physics of the Earth and Planetary Interiors*, *299*, 106409. https://doi.org/10.1016/j.pepi.2019.106409

Huang, Y., Strati, V., Mantovani, F., Shirey, S. B., & McDonough, W. F. (2014). Regional study of the Archean to Proterozoic crust at the Sudbury Neutrino Observatory (SNO+), Ontario: Predicting the geoneutrino flux. *Geochemistry, Geophysics, Geosystems*, *15*(10), 3925–3944. https://doi.org/10.1002/2014GC005397

Knudsen, P. (1987). Estimation and modelling of the local empirical covariance function using gravity and satellite altimeter data. *Bulletin Geodesique*, *61*(2), 145–160. https://doi.org/10.1007/bf02521264

Lemke, K., Hetényi, G., Secrétan, A., Li, J., Greenwood, A., Caspari, E., et al. (2026). Thermal properties of the lower continental crust: Variabilities and link to other rock properties based on DIVE drill cores and boreholes (Ivrea-Verbano zone). *Geothermics*, *136*, 103564. https://doi.org/10.1016/j.geothermics.2025.103564

Mancinelli, P., Porreca, M., Pauselli, C., Minelli, G., Barchi, M. R., & Speranza, F. (2019). Gravity and magnetic modeling of Central Italy: Insights into the depth extent of the seismogenic layer. *Geochemistry, Geophysics, Geosystems*, *20*(4), 2157–2172. https://doi.org/10.1029/2018GC008002

Mele, G., & Sandvol, E. (2003). Deep crustal roots beneath the northern Apennines inferred from teleseismic receiver functions. *Earth and Planetary Science Letters*, *211*(1–2), 69–78. https://doi.org/10.1016/S0012-821X(03)00185-7

Mele, G., Sandvol, E., & Cavinato, G. P. (2006). Evidence of crustal thickening beneath the central Apennines (Italy) from teleseismic receiver functions. *Earth and Planetary Science Letters*, *249*(3–4), 425–435. https://doi.org/10.1016/j.epsl.2006.05.024

Mirabella, F., Barchi, M., Lupattelli, A., Stucchi, E., & Ciaccio, M. G. (2008). Insights on the seismogenic layer thickness from the upper crust structure of the Umbria-Marche Apennines (central Italy). *Tectonics*, *27*(1), TC1010. https://doi.org/10.1029/2007TC002134

Mirabella, F., Brozzetti, F., Lupattelli, A., & Barchi, M. R. (2011). Tectonic evolution of a low-angle extensional fault system from restored cross-sections in the Northern Apennines (Italy). *Tectonics*, *30*(6), TC6002. https://doi.org/10.1029/2011TC002890

Montone, P., & Mariucci, M. T. (2020). Constraints on the structure of the shallow crust in Central Italy from geophysical log data. *Scientific Reports*, *10*(1), 3834. https://doi.org/10.1038/s41598-020-60855-0

Montone, P., & Mariucci, M. T. (2026). Rock densities from deep well sonic logs in Central Italy [Dataset]. *Zenodo*. https://doi.org/10.5281/zenodo.19096119

Moritz, H. (1980). *Advanced physical geodesy*. Abacus Press, Tunbridge Wells.

Navas, S., Amsler, C., Gutsche, T., Hanhart, C., Hernández-Rey, J., Lourenço, C., et al. (2024). Review of particle physics. *Physical Review D*, *110*(3), 030001. https://doi.org/10.1103/PhysRevD.110.030001

Nicolai, C., & Gambini, R. (2007). Structural architecture of the Adria platform-and-basin system. *Bollettino della Societa Geologica Italiana*, *7*, 21–37.

Particle Data Group. (2025). Review of particle physics: 2025 update. Retrieved from https://pdg.lbl.gov/2025/

Patacca, E., & Scandone, P. (2007). Geology of the southern Apennines. *Bollettino della Societa Geologica Italiana*, *7*, 75–119.

Peccerillo, A. (2017). Cenozoic volcanism in the Tyrrhenian Sea region. In *Advances in volcanology* (2nd ed.). Springer. https://doi.org/10.1007/978-3-319-42491-0

Piana Agostinetti, N., & Amato, A. (2009). Moho depth and Vp/Vs ratio in peninsular Italy from teleseismic receiver functions. *Journal of Geophysical Research*, *114*, B06303. https://doi.org/10.1029/2008JB005899

Piana Agostinetti, N., Buttinelli, M., & Chiarabba, C. (2022). Deep structure of the crust in the area of the 2016-2017 Central Italy seismic sequence from receiver function analysis. *Tectonophysics*, *826*, 229237. https://doi.org/10.1016/j.tecto.2022.229237

Pola, A., Crosta, G. B., Fusi, N., & Castellanza, R. (2014). General characterization of the mechanical behaviour of different volcanic rocks with respect to alteration. *Engineering Geology*, *169*, 1–13. https://doi.org/10.1016/j.enggeo.2013.11.011

Reguzzoni, M., Rossi, L., Baldoncini, M., Callegari, I., Poli, P., Sampietro, D., et al. (2019). GIGJ: A crustal gravity model of the Guangdong Province for predicting the geoneutrino signal at the JUNO experiment. *Journal of Geophysical Research: Solid Earth*, *124*(4), 4231–4249. https://doi.org/10.1029/2018JB016681

Rossi, L. (2017). *Bayesian gravity inversion by Monte Carlo methods. PhD Thesis*. Politecnico di Milano.

Rossi, L., Reguzzoni, M., Sampietro, D., & Sansò, F. (2015). Integrating geological prior information into the inverse gravimetric problem: The Bayesian approach. In *VIII Hotine-Marussi symposium on mathematical geodesy. Int. Assoc. Geod. Symp. 142* (pp. 317–324). Springer. https://doi.org/10.1007/1345_2015_57

Sampietro, D., Capponi, M., Triglione, D., Mansi, A. H., Marchetti, P., & Sansò, F. (2016). GTE: A new software for gravitational terrain effect computation: Theory and performances. *Pure and Applied Geophysics*, *173*(7), 2435–2453. https://doi.org/10.1007/s00024-016-1265-4

Sansò, F., & Sideris, M. G. (2012). The local modelling of the gravity field by collocation. In *Geoid determination: Theory and methods, lecture notes in Earth System sciences* (Vol. 110, pp. 203–258). Springer. https://doi.org/10.1007/978-3-540-74700-0_5

Scisciani, V., Agostini, S., Calamita, F., Pace, P., Cilli, A., Giori, I., & Paltrinieri, W. (2014). Positive inversion tectonics in foreland fold-and-thrust belts: A reappraisal of the Umbria-Marche Northern Apennines (Central Italy) by integrating geological and geophysical data. *Tectonophysics*, *637*, 218–237. https://doi.org/10.1016/j.tecto.2014.10.010

Scrocca, D., Sciamanna, S., Di Luzio, E., Tozzi, M., Nicolai, C., & Gambini, R. (2007). Structural setting along the CROP-04 deep seismic profile (Southern Apennines-Italy). *Bollettino della Societa Geologica Italiana*, *7*, 283–296.

Spada, M., Bianchi, I., Kissling, E., Agostinetti, N. P., & Wiemer, S. (2013). Combining controlled-source seismology and receiver function information to derive 3-D Moho topography for Italy. *Geophysical Journal International*, *194*(2), 1050–1068. https://doi.org/10.1093/gji/ggt148

Strati, V., Wipperfurth, S. A., Baldoncini, M., McDonough, W. F., Gizzi, S., & Mantovani, F. (2020). Geoneutrinos from the rock overburden at SNO+. *Journal of Physics: Conference Series*, *1342*(1), 012020. https://doi.org/10.1088/1742-6596/1342/1/012020

Strati, V., Wipperfurth, S. A., Baldoncini, M., McDonough, W. F., & Mantovani, F. (2017). Perceiving the crust in 3-D: A model integrating geological, geochemical, and geophysical data. *Geochemistry, Geophysics, Geosystems*, *18*(12), 4326–4341. https://doi.org/10.1002/2017GC007067

Strumia, A., & Vissani, F. (2003). Precise quasielastic neutrino/nucleon cross-section. *Physics Letters B*, *564*(1–2), 42–54. https://doi.org/10.1016/S0370-2693(03)00616-6

Tadiello, D., & Braitenberg, C. (2021). Gravity modeling of the Alpine lithosphere affected by magmatism based on seismic tomography. *Solid Earth*, *12*(2), 539–561. https://doi.org/10.5194/se-12-539-2021

Takeuchi, N., Ueki, K., Iizuka, T., Nagao, J., Tanaka, A., Enomoto, S., et al. (2019). Stochastic modeling of 3-D compositional distribution in the crust with Bayesian inference and application to geoneutrino observation in Japan. *Physics of the Earth and Planetary Interiors*, *288*, 37–57. https://doi.org/10.1016/j.pepi.2019.01.002

Tarquini, S., Isola, I., Favalli, M., Battistin, A., & Dotta, G. (2023). TINITALY, a digital elevation model of Italy with a 10 meters cell size (version 1.1) [Dataset]. *Istituto Nazionale di Geofisica e Vulcanologia (INGV)*. https://doi.org/10.13127/tinitaly/1.1

Tavani, S., Petracchini, L., Billi, A., Carminati, E., Molli, G., Palano, M., et al. (2026). Lower-crustal unzipping drives active orogenic deformation. *Communications Earth & Environment*. https://doi.org/10.1038/s43247-026-04021-w

Tiberti, M. M., Buttinelli, M., Maesano, F. E., Ferri, F., De Gori, P., Minelli, L., et al. (2026). 2D gravity modelling in Central Italy: Clues for the seismogenesis in the Apennines. *Tectonophysics*, *926*, 231113. https://doi.org/10.1016/j.tecto.2026.231113

Vai, G. B. & Martini, I. P. (Eds.) (2001). *Anatomy of an Orogen: The Apennines and adjacent Mediterranean basins*. Kluwer Academic Publishers. https://doi.org/10.1007/978-94-015-9829-3

Zingerle, P., Pail, R., Gruber, T., & Oikonomidou, X. (2020). The combined global gravity field model XGM2019e. *Journal of Geodesy*, *94*(7), 66. https://doi.org/10.1007/s00190-020-01398-0